RESEARCH ARTICLE

Fault geometry of M6-class normal-faulting earthquakes in the outer trench slope of Japan Trench from ocean bottom seismograph observations

Koichiro Obana[*] , Tsutomu Takahashi, Yojiro Yamamoto, Takeshi Iinuma, Yasuyuki Nakamura, Gou Fujie, Seiichi Miura and Shuichi Kodaira

Abstract

Since the 2011 Mw 9.0 Tohoku-oki earthquake, intra-plate normal-faulting earthquakes, including several M7-class earthquakes, have occurred in the outer trench slope area from the trench to the outer rise along the Japan Trench. Concerns regarding large earthquakes and associated tsunamis have also arisen. Based on aftershock distributions, several outer trench slope normal-faulting earthquakes (hereinafter referred to as outer-rise earthquakes) are likely related to the rupture of multiple faults. However, few observations have clearly shown how multiple faults act during outer-rise earthquakes. During the ocean bottom seismograph (OBS) observations in the outer trench slope area of the central Japan Trench from September 2017 to July 2018, three M6-class normal-faulting earthquakes (Mw 6.2 on September 20, Mw 6.2 on October 06, and Mw 6.0 on November 12) occurred around the OBS network. The near-field OBS observations provided detailed information on hypocenter locations and focal mechanisms of the mainshocks and aftershocks, including immediately after the mainshocks. We investigated the fault configurations of normal-faulting earthquakes based on OBS observations. During the September 2017 earthquake, the mainshock ruptured high-angle normal faults with a dip angle of 65°. Off-fault aftershock activities that were not directly related to the mainshock rupture and could be explained by the stress changes caused by the mainshock were confirmed. However, hypocenter distributions and focal mechanisms of the main and aftershocks of the October and November 2017 earthquakes suggest that the mainshock ruptured multiple faults with various dipping directions, angles, and strike orientations. The complicated fault geometry should be considered a possible fault model for large outer-rise earthquakes and related tsunamis.

Keywords Outer trench slope, Japan Trench, Outer-rise normal-faulting earthquake, Pacific Plate, Stress change, Seismicity

1 Introduction

The 2011 Tohoku-oki Mw 9.0 earthquake ruptured the interplate mega-thrust fault in the Japan Trench subduction zone, where the incoming Pacific plate subducts beneath northeast Japan, with a maximum slip greater than 50 m (e.g., Sun et al. 2017; Wang et al. 2018). After the 2011 earthquake, intra-plate normal-faulting earthquakes, including several M7-class earthquakes, occurred beneath the outer trench slope area from the

*Correspondence:
Koichiro Obana
obanak@jamstec.go.jp
Research Institute for Marine Geodynamics (IMG), Japan Agency for Marine-Earth Science and Technology (JAMSTEC), 3173-25 Showa-machi, Kanazawa-ku, Yokohama, Kanagawa 236-0001, Japan

Obana *et al. Progress in Earth and Planetary Science*   (2023) 10:11

Page 2 of 19

trench axis to the outer rise of the incoming Pacific Plate along the Japan Trench (e.g., Asano et al. 2011; Nakamura et al. 2016) (Fig. 1). Aftershock activity seaward from the trench is often associated with shallow mega-thrust slips (Sladen and Trevisan 2018). The outer-rise normal-faulting activities were concentrated in the central Japan Trench, where the large (> 5 m) coseismic slip occurred on near-trench mega-thrust during the 2011 Tohoku-oki earthquake (Iinuma et al. 2012). Overall activity, however, spanned between 36° and 41° N (Fig. 1). The extent of the outer trench slope normal-faulting aftershocks of the 2011 Tohoku-oki earthquake is quite remarkable. Similarly, in the 2007–2008 Kuril earthquake sequence, a Mw 8.3 mega-thrust event was followed by a Mw 8.1 outer trench slope normal-faulting event two months later (Lay et al. 2020).

Regarding the outer trench slope normal-faulting earthquakes (hereinafter referred to as outer-rise earthquakes), the concern of large earthquakes and related tsunamis after the 2011 earthquake has been raised, similar to several previous earthquake sequences, such as the 1896 Meiji-Sanriku tsunami earthquake (M ~8.0, Tanioka and Satake 1996) in the northern Japan Trench, which was followed by the 1933 Showa-Sanriku outer-rise earthquake (Mw 8.4, Kanamori 1971) (e.g., Lay et al. 2011) (Fig. 1). Although large outer-rise earthquakes are relatively infrequent compared with subduction mega-thrust earthquakes, they can cause devastating tsunami damage comparable to that of a mega-thrust earthquake, as was the case with the 1933 Showa-Sanriku earthquake, which caused approximately 3000 fatalities. (e.g., Headquarters for Earthquake Research Promotion 2009). Considering the increased seismicity in the Japan Trench after the 2011 Tohoku-oki earthquake, evaluation of the earthquake and tsunami hazard should consider outer-rise earthquakes and associated tsunamis.

Fault geometry is an important factor in evaluating tsunamis generated by outer-rise earthquakes. The propagation direction of tsunami wave energy and tsunami heights along the coast are affected by strikes and dip angles of faults (Álvarez-Gómez et al. 2012; Baba et al. 2020). However, owing to the lack of near-field
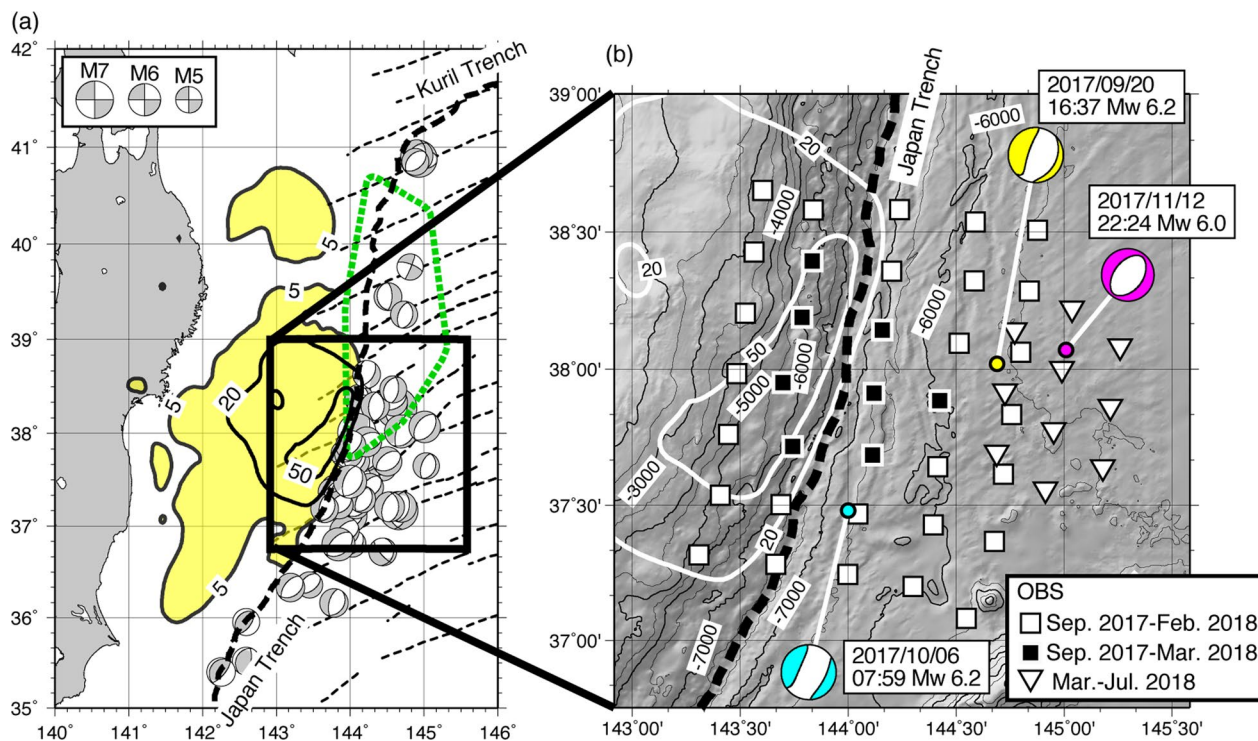

Fig. 1 Map of the survey area in the trench and outer trench slope of the central Japan Trench. **a** GCMT solutions (Dziewonski et al. 1981; Ekström et al. 2012) for Mw ≥ 5.0 earthquakes from March 11, 2011, to December 2021. Only GCMT solutions located on the seaward side of the trench axis are plotted. The yellow shaded region is the coseismic slip area of the 2011 Tohoku-oki earthquake with 5-, 20-, and 50-m contours (Iinuma et al. 2012). The thick black dashed line indicates the Japan and Kuril trench axes. Thin dashed lines are the magnetic anomaly lineations (Nakanishi 2011). The dashed green line indicates the 3-month outer-trench aftershock area of the 1933 Showa-Sanriku earthquake (Uchida et al. 2016). **b** Close-up view of the survey area. OBS locations are indicated with black and white squares and inverted triangles for different observation periods. Focal mechanisms of three M6-class earthquakes in 2017 taken from the GCMT catalog (Dziewonski et al. 1981; Ekström et al. 2012) are indicated. White contours indicate 20-m and 50-m contours of the coseismic slip distribution of the 2011 Tohoku-oki earthquake (Iinuma et al. 2012)

observations for outer-rise earthquakes, which occur far offshore from the coast, it is generally difficult to constrain fault geometries. For the 1933 Showa-Sanriku earthquake, Kanamori (1971) proposed a westward-dipping normal fault with a dip angle of 45° and fault size of 185×100 km^2 from seismic waveform data. However, Abe (1978) pointed out that such a fault could not explain the initial motion of the observed tsunamis and proposed a lower dipping angle of 30°. In contrast, Uchida et al. (2016) proposed a compound rupture of two trench-parallel normal faults with different dipping directions: westward-dipping and eastward-dipping, based on the relocated hypocenters of the mainshock and 3-month aftershocks. They showed that the simultaneous rupture of these two normal faults with a fault strike parallel to the trench could explain the observed tsunami first motions.

The bathymetric features in the outer trench slope region of the Japan Trench show both westward- and eastward-dipping normal faults forming horst-graben structures, which are generally parallel to the trench and created in the outer trench slope area because of the bending of the oceanic plate (Nakanishi 2011). In addition, structures oblique to the trench but parallel to the magnetic anomaly lineations suggest deformations using abyssal hill fabrics, which were created parallel to the spreading centers (Nakanishi 2011) (Fig. 1). These bathymetric features in outer trench slope suggest complex deformations of the oceanic plate associated with normal faults with various fault geometries. However, few observations have clearly shown how multiple faults act during outer-rise earthquakes.

The compound rupture model of the 1933 earthquake proposed by Uchida et al. (2016) is based on relocated hypocenters and tsunami first-motion polarities. However, hypocenters were estimated from data recorded at onshore stations at least 200 km from the source area. Therefore, detailed fault geometry cannot be constrained. Aftershock activities along multiple faults were also observed using near-field ocean bottom seismograph (OBS) observations for some outer-rise earthquakes. For the 2010 Mw 7.4 outer-rise earthquake east of the Izu-Ogasawara trench, aftershock activities along three parallel lineations were observed through OBS observations (Obana et al. 2014). These lineations were oblique to the trench but perpendicular to the magnetic anomaly lineations. Therefore, these activities are likely related to preexisting faults associated with the fracture zones. In the outer trench slope area of the Japan Trench, Hino et al. (2009) presented the aftershock distribution along two conjugate normal faults from the OBS observations for the 2005 Mw 7.0 earthquake. Also, aftershock activity along two conjugate strike-slip faults was observed for

the July 2011 Mw 7.0 intra-plate strike-slip earthquake near the Japan Trench axis (Obana et al. 2013). Although the 2011 Mw 7.0 earthquake occurred ~50 km landward of the trench axis, an extensional stress regime similar to outer-rise normal-faulting earthquakes is expected from the focal mechanisms of the mainshock and aftershocks. Kubota et al. (2015) presented that the 2011 Mw 7.0 earthquake likely ruptured two conjugate strike-slip faults based on near-field ocean bottom pressure records. However, OBS observations for outer-rise earthquakes are generally conducted at a certain time after the mainshock. Aftershock area expansion was observed for the 2010 Izu-Ogasawara outer-rise earthquake (Obana et al. 2013). In addition, off-fault aftershocks can be triggered by mainshocks (e.g., Das and Henry 2003). Hence, the geometry of the source faults of outer-rise earthquakes is not evident from the aftershock distributions at a certain time after the mainshock. The near-field observations for the mainshock and aftershocks immediately after the mainshock illuminate the detailed aspects of the fault geometry of the outer-rise earthquakes.

In this study, we investigated the fault geometries of outer-rise earthquakes based on OBS observations along the Japan Trench conducted from September 2017 to July 2018 (Fig. 1). During our observation period, three M6-class normal-faulting earthquakes, Mw 6.2 on September 20, Mw 6.2 on October 06, and Mw 6.0 on November 12 (Mw are according to the Global CMT (GCMT) catalog, Dziewonski et al. 1981; Ekström et al. 2012), occurred in the survey area. We observed the mainshocks and aftershocks for these earthquakes using the OBSs deployed near the source area. Based on these near-field OBS observations, we investigated the fault geometries and interactions of the outer-rise earthquakes, including the rupture of multiple faults in a complex fault system.

2 Methods
2.1 Observations
We conducted earthquake observations in the trench axis and outer trench slope area of the central Japan Trench from 2017 to 2018 (Fig. 1). We deployed 35 OBSs in September 2017 using the R/V Yokosuka (Japan Agency for Marine-Earth Science and Technology, JAMSTEC). In total, 27 of these OBSs were recovered by the R/V Yokosuka in February 2018. In March 2018, Kaiyo-maru No. 7 (Kaiyo Engineering Co. Ltd., Tokyo, Japan) recovered the remaining 8 OBSs and deployed 10 around the source area of the Mw 6.0 earthquake that occurred in November 2017. These 10 OBSs were recovered by Kaiyo-maru No. 2 (Kaiyo Engineering Co. Ltd.) in July 2018. In these observations, the horizontal spacing between OBSs was approximately 25−35 km.

We used two types of OBSs: a conventional type of OBS using a glass sphere as the pressure housing and ultra-deep-type OBSs using a ceramic pressure housing. The operation of the conventional OBSs is limited to depths shallower than 6000 m, although the trench axis in the survey area is deeper than 7000 m. We deployed ultra-deep OBSs along the trench axis. Each OBS was equipped with a three-component 4.5-Hz short-period seismometer, and conventional OBSs were also equipped with a hydrophone. Signals were sampled at a sampling frequency of 100 Hz using a 24-bit analog-to-digital converter and were recorded continuously. The internal clock drifts of the OBSs were corrected using linear interpolation of the time differences to the GPS-based reference clock, measured just before deployment and soon after recovery.

2.2 Analysis

Seismic events were detected from the continuous OBS record based on the amplitude ratio of the short-term average to the long-term average (STA/LTA). We also visually inspected the continuous seismic record from 1 day before to 3 days after the three M6-class earthquakes to identify small events that were not detected through STA/LTA. We manually picked P- and S-wave arrival times for seismic events using the *WIN* system (Urabe and Tsukada 1992). Where possible, the polarities of the P-wave first motion and maximum amplitudes were also picked from the vertical component seismograms.

Hypocenter locations were estimated from double-difference analysis (Zhang and Thurber 2003) following the procedures used in a previous study in the trench and outer trench slope area of the central Japan Trench (Obana et al. 2019). We determined the initial hypocenter locations using the hypomh program (Hirata and Matsu'ura 1987) (Additional file 1: Fig. S1). Two different 1-D P-wave velocity (Vp) models were used, depending on whether the station location was seaward or landward of the trench axis. Both Vp models were based on previous studies in the Japan Trench area (Ito et al. 2005; Hino et al. 2009). A fixed Vp/Vs of 1.78 was used for all OBSs. Although the 1-D Vp models do not include a low-velocity sedimentary layer beneath the OBSs, arrival time delays due to the sedimentary layer were corrected using station corrections. Station corrections were estimated from the arrival time differences between the direct P-wave arrivals and P-to-S converted phases at the bottom of the sedimentary layer. The Vp of the sedimentary layer was uniformly assumed to be 2.0 km/s, while two different values of Vp/Vs were adopted depending on whether the OBS was placed on the landward or seaward side of the trench axis. Vp/Vs values of 4.4 and 8.0 were assumed for the OBSs on the landward and seaward of

the trench axis, respectively, based on previous studies in the Japan Trench (Obana et al. 2019, 2021). The estimated station corrections were 0.032−0.210 s and 0.526−1.737 s for the P- and S-wave arrivals, respectively.

Initial hypocenter locations were obtained for more than 15,000 earthquakes, and we selected 6791 events to relocate using the 3-D seismic velocity model (Additional file 1: Fig. S1). The event selection was based on the following criteria: (1) Both P- and S-wave arrivals were picked for at least eight stations for events detected by STA/LTA or five stations for visually identified events before and after the M6-class earthquakes. (2) The maximum azimuthal gap of the stations with arrival time pick is ≤ 180°, or the initial hypocenters are located within 35 km from the nearest station. These events were relocated using the double-difference tomography method (Zhang and Thurber 2003). In the double-difference analysis, the velocity model configurations and initial velocities were the same as those used in a previous study by Obana et al. (2019) (Additional file 1: Fig. S2). We adopted station corrections similar to the initial hypocenter determination to correct the arrival time delay owing to the low-velocity sedimentary layer below the OBSs. The spatial resolution of the tomographic analysis was examined using a checkerboard resolution test. We applied ±5% velocity perturbations within alternating cells at 25 km intervals in the horizontal direction and 6–20 km in the vertical direction. Errors in hypocenter locations and velocity models were also estimated using 100 bootstrap samples.

We estimated the magnitudes and focal mechanisms based on hypocenter locations obtained from the double-difference analysis. The magnitudes of the events were estimated from the maximum amplitude of the vertical component seismograms using an equation for regional earthquakes (Watanabe 1971). Focal mechanisms were estimated from the first-motion polarities of the vertical seismograms using the HASH program (Hardebeck and Shearer 2002).

3 Results

We obtained hypocenter locations for 6784 earthquakes, 6261 of which were estimated with location errors of less than 5 km (Fig. 2a, b, and Additional file 1: Fig. S4). Approximately 68% of the hypocenters (4302 events) were estimated with location errors of less than 2 km. The velocity structure obtained from the tomographic analysis was generally consistent with a previous study based on OBS observations from 2011 to 2014 (Obana et al. 2019) (Additional file 1: Fig. S3a–c). The seismic velocity in the uppermost oceanic mantle of the incoming Pacific Plate decreases with proximity to the trench axis. The checkerboard pattern was recovered at depths
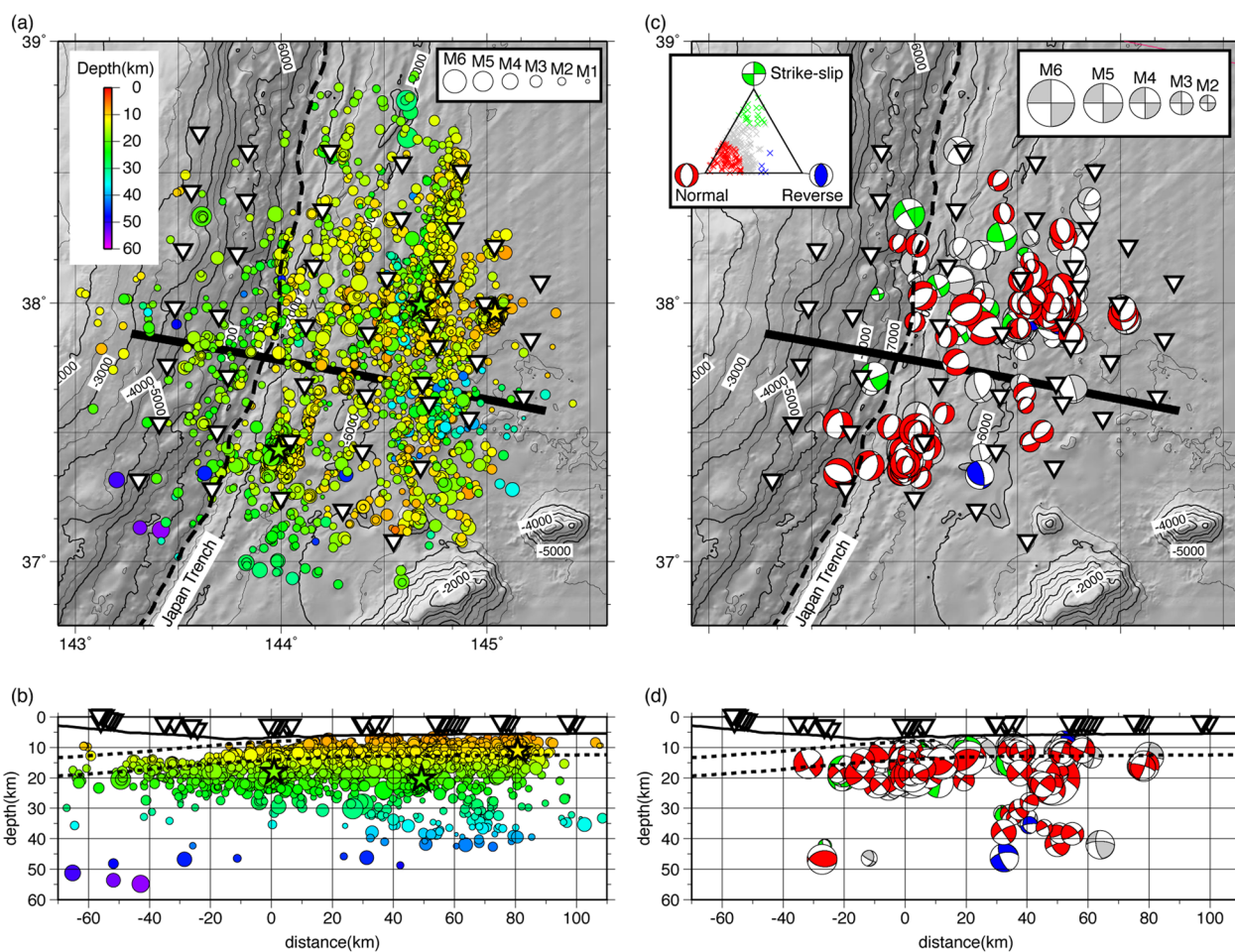
Fig. 2 Hypocenter distributions and focal mechanisms based on the tomographic analysis. **a** Map showing the hypocenters with location errors less than 5 km. Three M6-class earthquakes and others are indicated by stars and circles, respectively. The symbols are color-coded by hypocenter depth. Inverted triangles indicate the OBS locations. **b** Hypocenter distribution projected along the profile is indicated by thick solid lines on panel (**a**). Dashed black lines indicate the top of the oceanic crust (Ito et al. 2005) and the approximate depth of the Moho, which is 7 km below the seafloor seaward of the trench and 6 km below the top of the oceanic crust landward of the trench. Inverted triangles indicate the projected locations of OBSs. **c** Focal mechanisms estimated from first-motion polarities observed by the OBSs. Focal mechanisms are color-coded according to the triangle diagram of Frohlich (1992), as presented in the inset panel. **d** Focal mechanisms projected along the profile indicated by the thick solid line on panel (**c**)

down to 40 km, although the patterns within the oceanic crust and the overriding plate landward of the trench axis were not recovered (Additional file 1: Fig. S3d–f).

The magnitudes of three M6-class earthquakes that occurred in 2017 (Mw 6.2 on September 20, Mw 6.2 on October 06, and Mw 6.0 on November 12, according to the GCMT) were estimated to be M 6.7, 6.6, and 6.4 from the OBS observations, respectively. The earthquake activities were not limited to the region surrounding the hypocenters of these three M6-class earthquakes. Active seismicity in the outer trench slope area can be observed within 110 km of the trench axis. This finding is similar to those of a previous study based on OBS observations from 2011 to 2014 (Obana et al. 2019). Most of the

earthquakes occurred at depths shallower than approximately 20 to 25 km, corresponding to the oceanic crust and the uppermost 10 km of the oceanic mantle. Some occurred at depths 50 km beneath the trench axis and the outer trench slope.

Focal mechanisms were obtained for 228 earthquakes with qualities A and B, as defined in the HASH program by Hardebeck and Shearer (2002), which correspond to fault plane uncertainties of $\leq 35°$ (Fig. 2c, d). According to the triangle diagram of Frohlich (1992) (inset of Fig. 2c), most earthquakes were classified as normal-faulting or intermediate focal mechanisms close to normal-faulting. The pre-dominance of normal-faulting earthquakes down to a depth of approximately 40 km is similar to the

Obana *et al. Progress in Earth and Planetary Science* (2023) 10:11

Page 6 of 19

findings of previous studies based on OBS observations after the 2011 Tohoku-oki earthquake (Obana et al. 2012, 2019).

4 Discussion

As described in the previous section, the overall results of the hypocenter distribution, focal mechanisms, and velocity structures are generally consistent with those of a previous study based on OBS observations from 2011 to 2014 by Obana et al. (2019). In the following discussions, we focus on the three M6-class earthquakes, Mw 6.2 on September 20, Mw 6.2 on October 06, and Mw 6.0 on November 12, and their aftershocks that occurred in 2017.

4.1 September 20, 2017 earthquake and its aftershocks

The rupture of the September 20, 2017 earthquake (Mw 6.2 from the GCMT and M 6.7 from the OBS observation) was initiated at a depth of 20 km, corresponding to the uppermost oceanic mantle of the Pacific plate (Fig. 3 and Additional file 1: Fig. S5). Aftershocks within a few hours of the mainshock (red circles in Fig. 3) were mainly located at depths of approximately 20 km and shallower than 13 km, corresponding to the uppermost mantle and oceanic crust, respectively. The aftershock activity extended along the NNE–SSW direction (Fig. 3a), parallel to the westward-dipping nodal plane of the GCMT solution. The focal mechanism of the mainshock from the OBS first-motion polarities and aftershock distribution suggests the rupture of a westward-dipping high-angle normal fault, which is consistent with the GCMT solution (Fig. 3d, e). The aftershocks within the uppermost oceanic mantle were aligned along a westward-dipping plane with a dip angle of 65°. Conversely, earthquakes within the oceanic crust seem to align along a steeper plane with a dip angle of 85° (Fig. 3).

Within 1 h of the mainshock, the aftershock area extended 10.3 km along the strike oriented to NNE–SSW and 14.2 km along the dip (gray-shaded area in Fig. 3c–e). For Mw 6.2 earthquake, the rupture area is expected to be 283.9 km² and 163.7 km² from the scaling relationships for large normal-faulting earthquakes (Álvarez-Gómez et al. 2012) and shallow continental normal-faulting earthquakes (Wells and Coppersmith 1994), respectively. Assuming that the 1-h aftershock area indicates the rupture extent of the mainshock, it can be considered a minimum estimation source fault extent compared to that expected from the magnitude scaling relationships. The centroid depth of the GCMT solution is located within the depth range of the 1-h aftershock area, although the horizontal location is slightly outside that area. Location errors of the GCMT solutions are expected to be approximately 10 km in horizontal direction and 5–8 km in depth (Hjörleifsdóttir and Ekström 2010). The GCMT location is consistent with the 1-h aftershock area within the expected errors. The westward-dipping nodal plane is also consistent with the aftershock distribution. Thus, we consider that the 1-h aftershock is indicative of the fault extent of the mainshock rupture.

The aftershock activities expanded both along and normal to the strike of the mainshock rupture fault beyond the 1-h aftershock area (Fig. 3 and Additional file 1: Fig. S5). These expanded activities were mainly observed within the oceanic crust. Along the strike of the mainshock fault (profile C–C' in Fig. 3c, g), the aftershock activity expanded approximately 10 km to the north for the first 8 h. Although aftershock activity to the south of the mainshock was less apparent, aftershock area expansion was also observed. The aftershocks were also activated in the east and west of the mainshock rupture (Fig. 3d). These aftershocks were located approximately 15–20 km west and within 10 km east of the mainshock rupture area. Aftershock activity west and east of the mainshock started approximately 1.6 h to 2.0 h after the mainshock and expanded in the NNE–SSW direction, parallel to the strike of the mainshock fault (Fig. 3f–h and Additional file 1: Fig. S5).

(See figure on next page.)
Fig. 3 Mainshock and aftershock activity of the September 20, 2017 earthquake. **a** Map showing epicenter distribution of the mainshock and aftershocks. The bathymetry relief is represented in grayscale based on the red relief map in Fig. 10b and c (Chiba et al. 2008). The earthquakes within the dashed rectangles are indicated by circles color-coded with time after the mainshock, as indicated in panel (**b**). The mainshock is marked with a green star. Other earthquakes before the mainshock and after September 23 are indicated with open circles. The focal mechanism of the mainshock from the GCMT catalog and OBS first-motion polarities are indicated. **b** Magnitude-time diagram of the earthquakes within the dashed rectangles on panel (**a**). **c** Cross sections of the hypocenters along the profile C–C' on panel (**a**). Earthquakes within 5 km from the profile (within the dashed rectangle) are projected. The gray rectangle indicates the area of the earthquakes that occurred within 1 h after the mainshock. The seafloor and the approximate depth of the Moho, 7 km below the seafloor, are indicated by solid and dashed lines, respectively. **d**, **e** Cross sections of the hypocenters along the profile A–A' on panel (**a**). The dashed green lines with black arrows are the projection of the westward-dipping planes along which the aftershocks are aligned. The focal mechanisms from the first-motion polarities observed by the OBSs are also indicated on panel (**e**). The OBS focal mechanisms are color-coded by the faulting types according to the triangle diagram of Frohlich (1992) as shown in Fig. 2. **f**–**h** Space-time plots of the mainshock and aftershocks projected along the profiles B–B' (**f**), C–C' (**g**), and D–D' (**h**). The gray-shaded region is the 1-h aftershock area along the profile C–C' (**g**), and its projection is on the other two profiles (**f**, **h**). Vertical dashed lines indicate the origin time of the mainshock and 2 h since
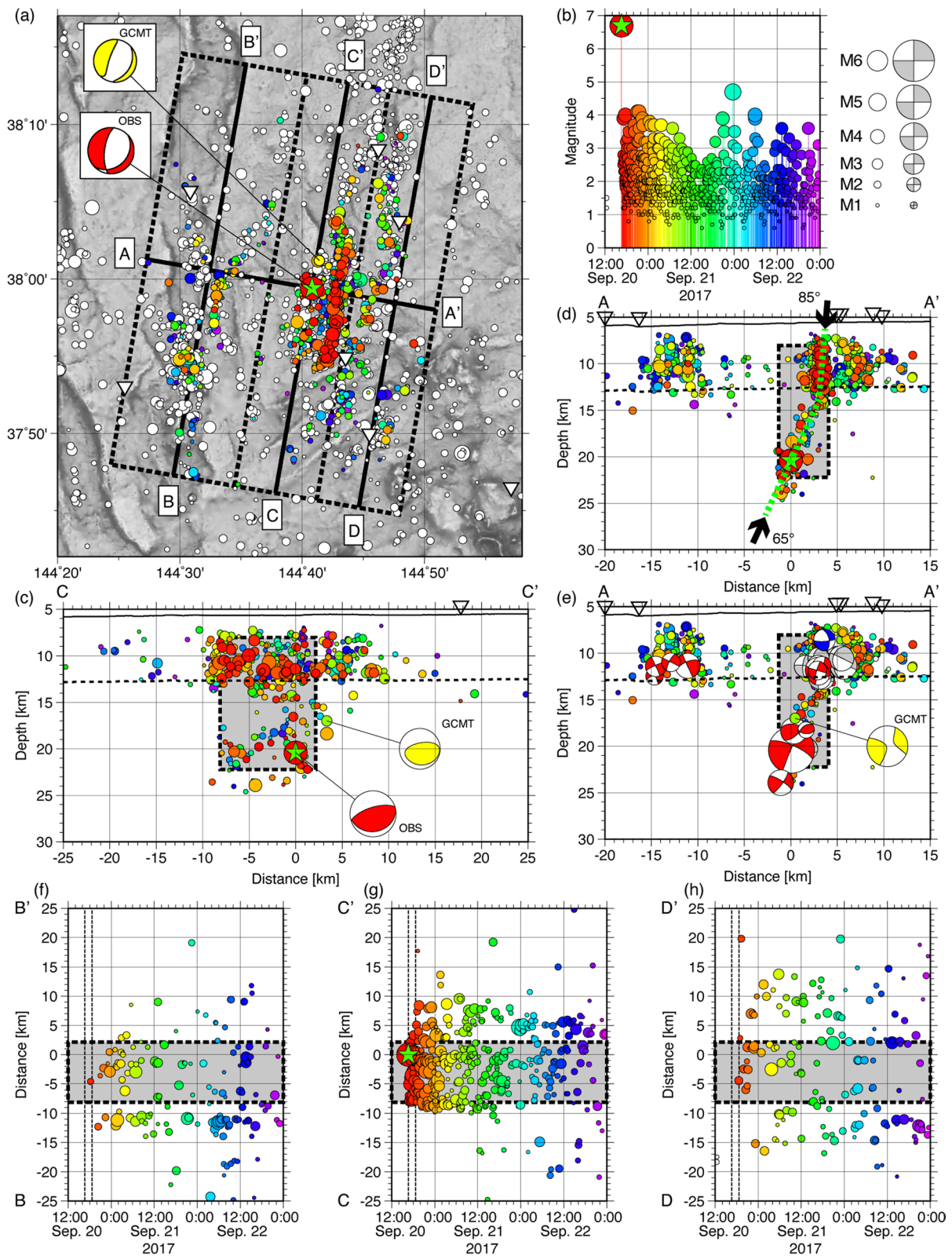
Fig. 3 (See legend on previous page.)

Considering the delayed activation of these two clusters east and west of the mainshock rupture, these clusters were not the activity of the source fault of the mainshock rupture. However, mainshock rupture can activate these off-fault aftershocks. We calculated the Coulomb stress changes caused by mainshock rupture using a formulation by Okada (1992) (Fig. 4). As the source fault of the mainshock, two models were examined: one in which the mainshock rupture extended both in the uppermost mantle and oceanic crust (case 1) (Fig. 4a, c) and the other in which the mainshock rupture only occurred in the uppermost oceanic mantle (case 2) (Fig. 4b, d). The geometry of the source fault is based on the 1-h aftershock distribution, and a pure normal fault slip with a rake angle of −90° was assumed (Table 1). The amount of slip was estimated to satisfy the seismic moment of 2.68 × 10^18 Nm from the GCMT solution with an assumed rigidity of 70 GPa. A frictional coefficient of 0.4 was adopted with reference to a previous study for aftershocks of the 2011 Tohoku-oki earthquake by Toda et al. (2011). The Coulomb stress changes were calculated for both westward- and eastward-dipping normal faults with a dip angle of 70° based on previous studies in the outer slope area of the Japan Trench (Obana et al. 2018; Park et al. 2021).

The estimated stress changes show that aftershocks generally occur in the increased stress regions. The off-fault aftershock activations are generally associated with a stress increase of 0.01 MPa (Harris 1998). Although it is difficult to identify the dip direction of the faults related to the off-fault aftershocks from the aftershock hypocenter distribution (Fig. 3d), the aftershocks 15–20 km west of the mainshock fault located in the area of stress increased over 0.01 MPa on both westward and eastward-dipping faults. However, more than 50% of the aftershocks east of the mainshock and along the mainshock fault were located where the stress decreased when the mainshock rupture extended both in the oceanic crust and uppermost mantle (case 1, Fig. 4a, c, and Additional file 1: Fig. S6, Additional file 2: Table S1). The stress increase on both westward- and eastward-dipping normal faults is expected to be 60–80% of the aftershock east of the mainshock and along the mainshock fault when the mainshock only ruptures the fault in the uppermost

oceanic mantle (case 2, Fig. 4b, d, and Additional file 1: Fig. S6, Additional file 2: Table S1). Few aftershocks generally occur in the region of large coseismic slip (e.g., Das and Henry 2003). Fewer aftershocks within the uppermost mantle than those in the oceanic crust (Fig. 3c) suggest that the main rupture occurred mainly on the fault within the uppermost oceanic mantle.

Our observations suggest that the September 2017 earthquake ruptured a westward-dipping high-angle normal fault with a slip that mostly occurred in the uppermost mantle. The off-fault aftershocks parallel to the mainshock fault can be activated by static stress changes caused by the mainshock rupture. This indicates that the compound rupture of multiple faults is not evident only from the overall distribution of aftershocks. However, for the 1933 Sanriku earthquake (Mw 8.4), a compound rupture of two normal faults with different dipping directions was proposed from the combined analysis of the aftershock distribution and tsunami waveforms (Uchida et al. 2016). Careful investigation of aftershock activities is necessary to examine the rupture of outer-rise earthquakes.

4.2 October 06, 2017 earthquake and its aftershocks

The rupture of the October 06, 2017 earthquake initiated at a depth of 18 km, and the aftershock area extended in the NNE–SSW direction, which is parallel to the general trend of the horst-graben structures in the source region (Fig. 5). The extent of the 1-h aftershock area is 10.0 km along the strike (profile B–B′ in Fig. 5a) and 11.0 km in depth. The spatial extent of the 1-h aftershock area is comparable to that of the September 2017 earthquake with the same moment magnitude of Mw 6.2. The aftershock area expanded approximately 10 km along the strike beyond the 1-h aftershock area 2 days after the mainshock (Fig. 5e). The fault plane is not apparent on the cross section of the aftershocks (Fig. 5c). The OBS first-motion focal mechanisms show many intermediate focal mechanisms with strike-slip components, such as the mainshock mechanism (Fig. 5a), as well as normal-faulting mechanisms (Fig. 5d).

The detailed distribution of the 1-h aftershocks suggests that the mainshock ruptured several faults with different dipping directions and angles (Fig. 6). The 1-h

(See figure on next page.)
Fig. 4 Coulomb stress changes on 70° dipping normal faults for the September 20, 2017 earthquake. Map views at a depth of 11 km and vertical cross sections along the profile indicated by thick solid lines in the map view, which is the same as the profile A–A′ in Fig. 3a, are shown. The stress change on westward- (**a**, **b**) and eastward-dipping (**c**, **d**) faults with a strike parallel to the mainshock is indicated. The stress changes are calculated for the mainshock fault when it ruptures in both the oceanic crust and uppermost mantle (case 1: **a**, **c**) and when it ruptures only in the uppermost mantle (case 2: **b**, **d**). Green stars are the hypocenter of the mainshock. The green rectangle on the map view and the thick green line on the cross sections are the assumed faults of the mainshock. The green dashed lines are the contour of a Coulomb stress increase of 0.01 MPa. Open circles are the aftershocks that occurred until September 22, 2017, which are the same as the colored events in Fig. 3. The aftershocks within the dotted rectangle on the map views are projected on the cross sections. The inverted triangles are the OBSs
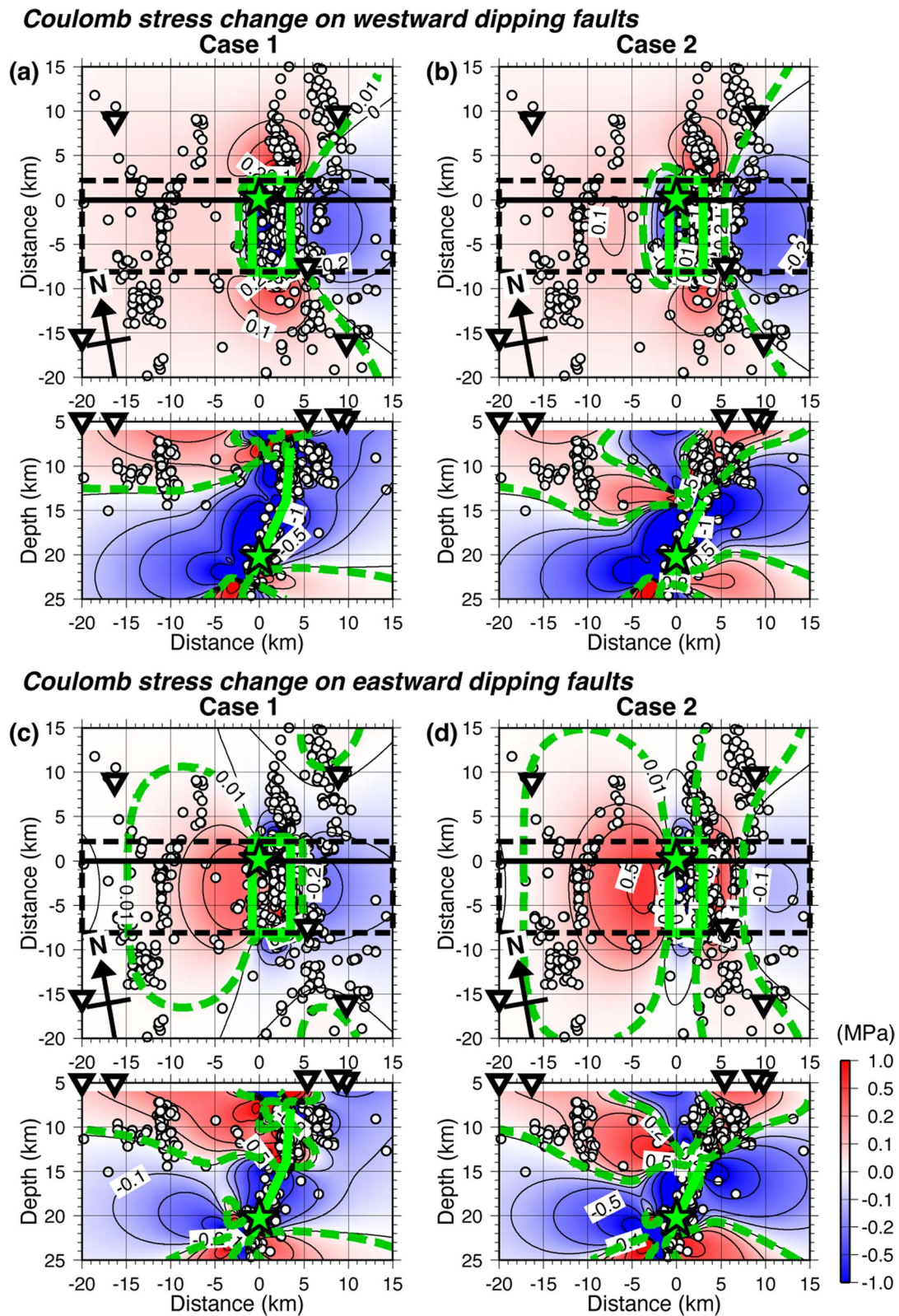
Fig. 4 (See legend on previous page.)

Table 1 Fault parameters of the September 20, 2017 earthquake

	Oceanic crust	Uppermost mantle
Depth of the updip end (km below sea level)	7.98	14.0
Dip (°)	85	65
Rake (°)	− 90	− 90
Length (km)	10.3	10.3
Width (km)	6.02	9.05
Case 1: slip (cm)	24.7	24.7
Case 2: slip (cm)	0.0	41.1

aftershocks occurred along the eastward- and westward-dipping planes with dip angles between 45° and 70°. The mainshock rupture initiated on the 65° eastward-dipping plane (red star on the E–E' profile in Fig. 6c). The aftershocks show a high-angle eastward-dipping plane to the south. In contrast, the dip angle of the eastward-dipping plane becomes shallower, at 45° to the north. In addition, there was a westward-dipping plane with a dip angle of 55°. The aftershocks within 1 h of the mainshock occurred on these eastward- and westward-dipping planes with various dip angles. Strike-slip and intermediate focal mechanisms with strike-slip components were
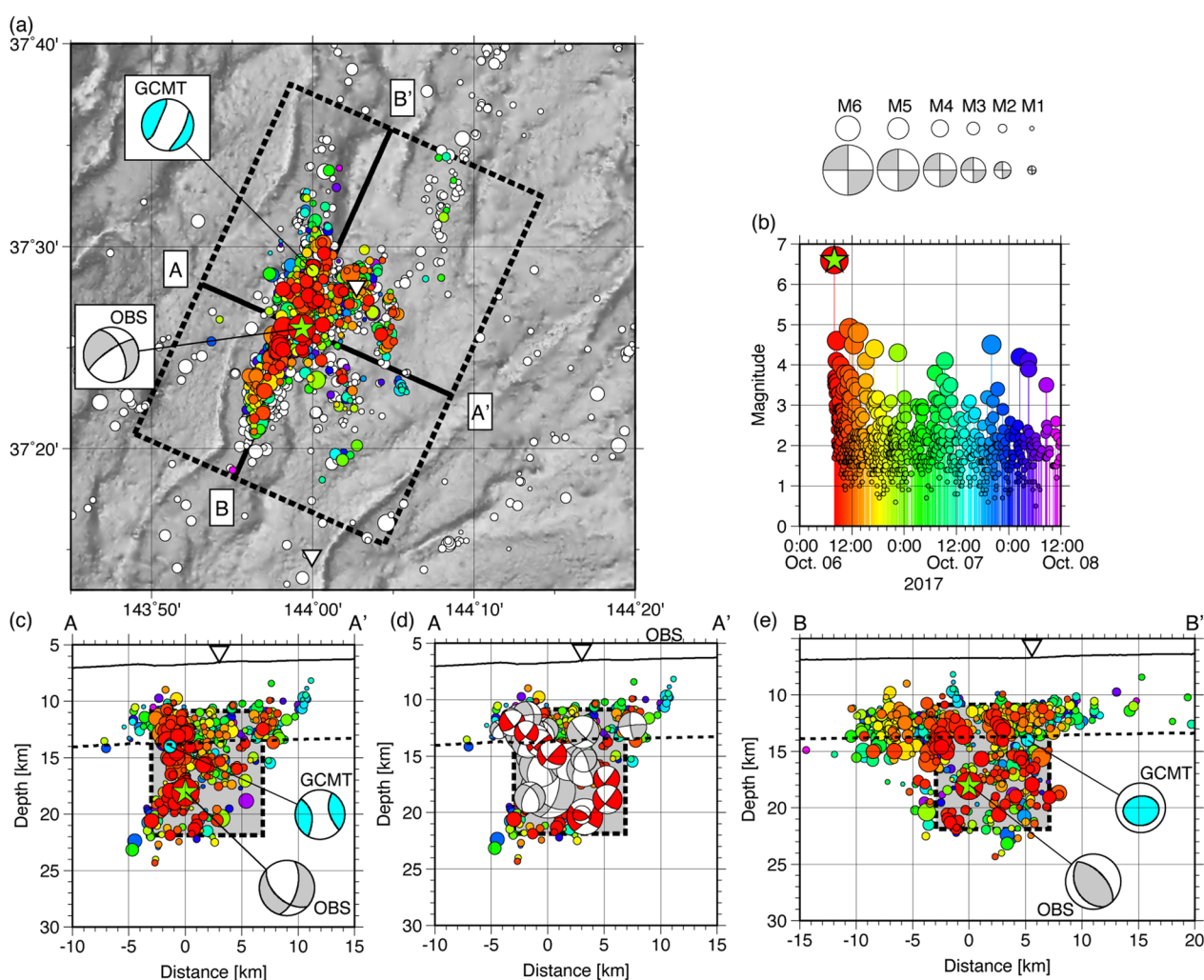

Fig. 5 Mainshock and aftershock activity of the October 06, 2017 earthquake. **a** Map showing the epicenter distribution of the October 06, 2017 earthquake and its aftershocks. The mainshock and aftershocks within the dashed rectangle are circles color-coded with time after the mainshock, as indicated in panel (**b**). The mainshock is marked with a green star. The focal mechanism of the mainshock from the GCMT catalog and OBS first-motion polarities are indicated. **b** Magnitude-time diagram of the earthquakes within the dashed rectangle on panel (**a**). **c**, **d** Cross sections of the hypocenters along the profile A–A' on panel (**a**). Focal mechanisms from the OBS first-motion polarities are also indicated on panel (**d**). The focal mechanisms are color-coded by the faulting types according to the triangle diagram of Frohlich (1992), as shown in Fig. 2. The gray rectangle indicates the area of the earthquakes that occurred within 1 h from the mainshock. **e** Cross sections of the hypocenters along the profile B–B' on panel (**a**)

concentrated in the 1-h aftershock area (sections C–C' to F–F' in Fig. 7). However, normal-faulting earthquakes occurred to the north and south of the 1-h aftershock area (Fig. 7). Thus, the source fault of the mainshock of the October 2017 earthquake likely had a complicated geometry consisting of multiple faults rather than a simple normal fault.

In the source area of the October 2017 earthquake, the strike of the horst-graben structures oriented in the NNE–SSW direction, which is generally parallel to the Japan Trench axis. These structures can be divided into small segments, and both eastward and westward escarpments have been identified from bathymetric data (Nakanishi 2011). Additionally, topographic features of NE–SW strikes have been identified in this area (Nakanishi 2011). These structures are parallel to the magnetic anomaly lineations and are related to the reactivation of abyssal hill fabrics formed at the spreading centers. The NE–SW strike nodal plane of the mainshock focal mechanism, estimated from the OBS first-motion polarities, suggests rupture along these structures. Structures with various strike orientations and dip directions in this region can promote the rupture of multiple faults with complicated geometries.

4.3 November 12, 2017 earthquake and its aftershocks

The rupture of the November 12, 2017 earthquake was initiated at a depth of 11 km. The aftershocks were located both in the oceanic crust and uppermost mantle (Fig. 8). The aftershock area extended approximately 10 km in the NE–SW direction (profile A–A' in Fig. 8), which is parallel to the strike of the GCMT solution, although the GCMT solution was located approximately 10 km away from the aftershock area. The cross section along the NW–SE profile (profile B–B' in Fig. 8) shows that the hypocenters of the mainshock and aftershocks were located generally along a northwestward-dipping plane with a dip angle of $45°$ (Fig. 8d). The extent of the 1-h aftershock area is approximately 9 km both along the NE–SW strike parallel to the GCMT solution and in depth. This is relatively smaller than that of the September and October 2017 earthquakes but is reasonable given the difference in moment magnitude (Mw 6.2 for the September and October 2017 earthquakes and Mw 6.0 for the November 2017 earthquake). The normal-faulting rupture on the northwestward-dipping plane is

consistent with the GCMT solution. The NE–SW direction is roughly parallel to the magnetic anomaly lineations (Nakanishi 2011) (Fig. 1). The mainshock rupture is likely related to the abyssal hill fabrics formed at the spreading centers.

Conversely, aftershocks within a few hours of the mainshock, including some larger aftershocks (M ~4, marked by thin arrows in Fig. 8d), were located below the northwestward-dipping plane. The E–W cross section along the profile C–C' (Fig. 8e) shows that these earthquakes and the rupture initiation of the mainshock were located along a westward-dipping plane with a dipping angle of $70°$. The focal mechanisms of the aftershocks suggest the rupture of the westward-dipping high-angle normal fault (Fig. 8f). Only two aftershock focal mechanisms were ranked as quality B for the November 2017 earthquake based on the OBS first-motion polarities. However, the first-motion polarities of the mainshock and some aftershocks suggest a complicated rupture of this earthquake. Figure 9 shows the first-motion polarities of the mainshock and seven aftershocks with focal mechanisms of quality B and D ranked by the HASH program (Hardebeck and Shearer 2002) that correspond to the fault plane uncertainties of $\leq 35°$ and $> 45°$, respectively. Because the OBSs were deployed only west of the aftershock area at the occurrence of this earthquake (Fig. 1), the focal mechanisms were not well constrained. Yet, the first-motion polarities for stations in the southwest direction show upward or downward motion, depending on the events. The variation in the first-motion polarities can be explained by activity along two normal faults with different strike orientations: NE–SW and N–S.

The GCMT solutions and NE–SW extending aftershocks indicate that the main rupture occurred on the fault parallel to the magnetic anomaly lineations oriented in NE–SW directions associated with the preexisting abyssal hill fabrics. In addition, the N–S extending trench-parallel fault was also related to the November 2017 earthquake. The first-motion polarities of the mainshock are similar to those of the focal mechanisms with quality B, which indicates normal-faulting with an N–S strike (Fig. 9). Normal faults with N–S strikes are likely associated with trench-parallel faults created in the outer trench slope area owing to the bending of the incoming Pacific plate. The November 12, 2017 earthquake occurred approximately 90 km east of the trench. Bending-related topographic features, such as

(See figure on next page.)
Fig. 6 Detailed distribution of the aftershocks of the October 06, 2017 earthquake. **a** The map indicates the profiles of the cross sections from A–A' to I–I' in panel (**c**). Horizontal intervals between the profiles are 2.5 km. The hypocenter of the mainshock is indicated by the red star on the profile E–E'. The aftershocks within 1 h after the mainshock are color-coded with time after the mainshock as shown in the magnitude-time diagram of panel (**b**). Other earthquakes are indicated with open circles. **b** Magnitude-time diagram of 1-h aftershock. **c** Cross sections along the profile A–A' to I–I' on panel (**a**). The aftershocks within 1 h after the mainshock are indicated by circles color-coded with the time after the mainshock. Earthquakes within the dotted rectangles are indicated on each cross section. Arrows indicate the dipping planes of the aftershocks
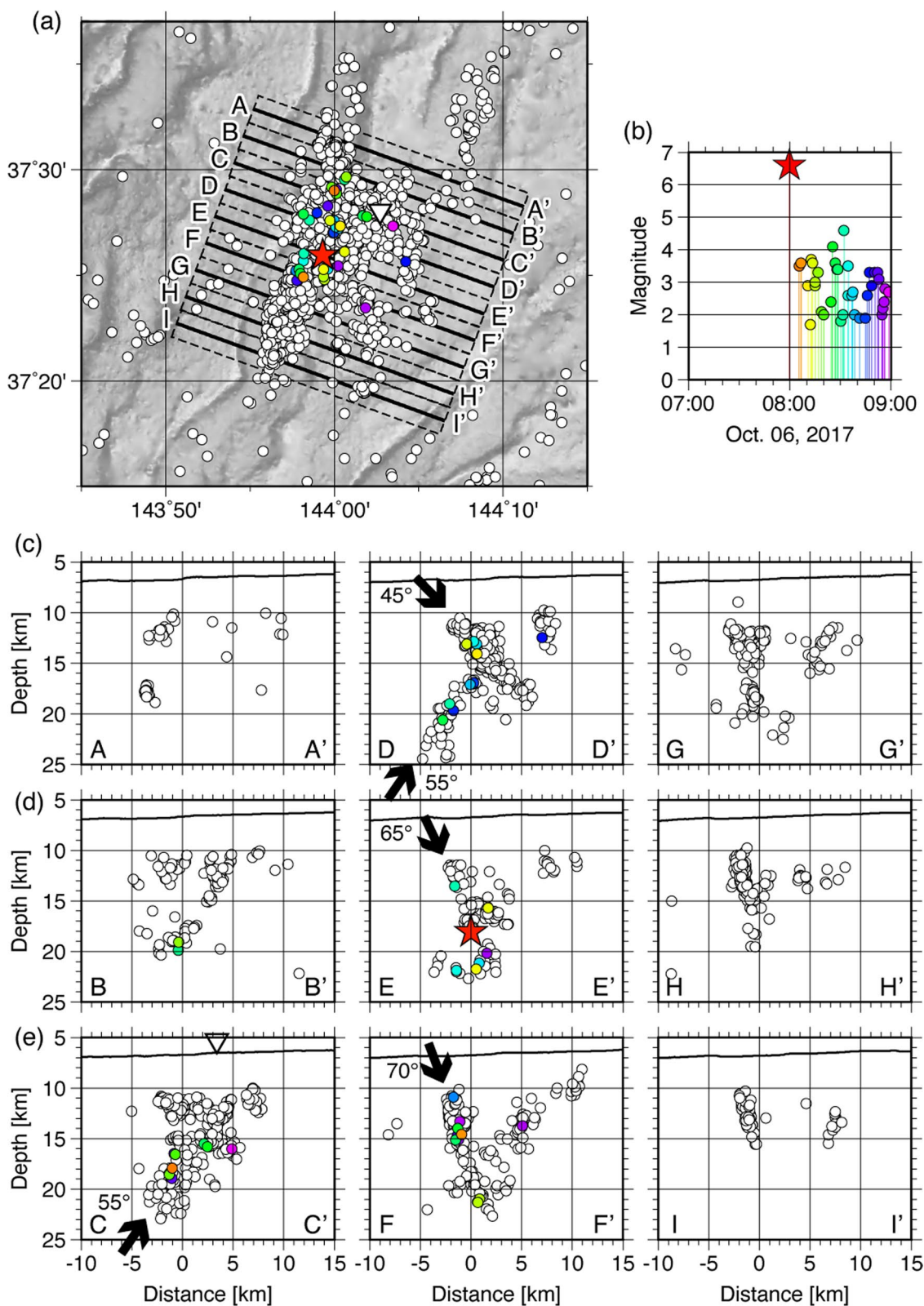
Fig. 6 (See legend on previous page.)

horst-graben structures, are apparent within 80 km of the trench axis (Nakanishi 2011). However, the focal mechanisms and first-motion polarities suggest that the deformation associated with trench-parallel normal faults occurred in the region where trench-parallel bending-related bathymetric features were not apparent. This means that outer-rise earthquakes consisting of multiple faults with different strikes and dip angles could have occurred in the region without clear bending-related topographic features.

4.4 Complex fault system in the outer trench slope of Japan Trench

The OBS observations in this study indicate that complex fault systems consisting of multiple faults with different dipping directions, angles, and fault strikes are related to the mainshock rupture and aftershock activity of three M6-class outer-rise earthquakes in the central Japan Trench. The outer-rise activities are likely associated with eastward- and westward-dipping normal faults forming horst-graben structures—which are generally parallel or sub-parallel to the trench axis—and reactivated abyssal hill fabrics, which are oblique to the trench but parallel to the magnetic anomaly lineations, in the Japan Trench outer-rise. Outer-rise normal-faulting activities after the 2011 Tohoku-oki earthquake mainly occurred in the central Japan Trench between 37° and 39° N, where significant coseismic slip (> 5 m) had occurred along the shallow near-trench mega-thrust (Iinuma et al. 2012) (Fig. 1). As discussed by Lay et al. (2020) and Sladen and Trevisan (2018), great mega-thrust earthquakes with ruptures extending to the trench are often associated with outer-rise normal-faulting activities because of the transient stress loading caused by mega-thrust slips. The complex fault systems of the outer-rise normal-faulting activities, including faults both parallel and oblique to the trench, could be activated by the stress changes related to the large slips on the shallow near-trench plate interface.

While the outer-rise normal-faulting activities after the 2011 Tohoku-oki earthquake concentrate in the central Japan Trench, previous OBS observations—including those conducted in northern (38.5°–40° N) and southern (36° −37.5° N) sections of the Japan Trench—indicate the outer-rise seismicity extended between 36° and 40° N, including the area without significant near-trench coseismic slip during the earthquake (Obana et al. 2018, 2019, 2021) (Fig. 10a). The OBS observations in the central Japan

Trench around 38° N have been repeated since the 2011 Tohoku-oki earthquake with total durations of approximately 2 years. In contrast, the observations in the northern and southern Japan Trench were conducted a single time each, with observation durations of 2 and 4 months, respectively. Therefore, it is difficult to directly compare the differences in seismic activity levels along the Japan Trench from the OBS observations. However, the OBS observations have revealed detailed hypocenter distributions of the active outer-rise seismicity extending along the Japan Trench after the 2011 Tohoku-oki earthquake as reported in land-based observation studies (Asano et al. 2011; Nakamura et al. 2016). After the 2011 Tohoku-oki earthquake, interplate slips on the shallow mega-thrust near the trench in latitudes below 37° N and over 39° N are expected from the seafloor geodetic observations (Iinuma et al. 2016; Honsho et al. 2019). In addition to the large coseismic slip during the 2011 Tohoku-oki earthquake, the transient stress changes caused by the postseismic slip related to the seamount subductions could enhance the outer-rise earthquake activities along the Japan Trench.

The earthquakes shallower than 14 km in depth, corresponding to the activity in the oceanic crust, show that there are linear earthquake trends of the outer-rise seismicity not only in the central Japan Trench around 38° N, but also in the northern and southern sections of the Japan Trench (Obana et al. 2018, 2021) (Figs. 10b, c). Although many linear trends can be seen in the central Japan Trench, only the ones identified by Obana et al. (2018, 2021) from the OBS observations in the northern and southern Japan Trench sections are marked in Fig. 10b and c. These 100- to 200-km-long linear earthquake trends are generally parallel or sub-parallel to the trench axis. In some parts, no clear faults can be identified in the bathymetry, but the earthquake trends span over multiple small segments of bending-related faults with various fault strikes including those oblique to the trench. Two of them north of 38° N (linear trend A and B in Fig. 10b) correspond to the aftershock activity of the 1933 Showa-Sanriku earthquake, which suggests the compound rupture of two normal faults with different dip directions (Uchida et al. 2016). Although detailed fault geometries are not constrained for the linear earthquake trends, these trends suggest the possible complex rupture of multiple faults during large

(See figure on next page.)
Fig. 7 Focal mechanisms in the source area of the October 06, 2017 earthquake. Hypocenters and focal mechanisms are indicated for the earthquakes that occurred during the entire observation period. **a** Map showing the focal mechanisms estimated from OBS first-motion polarities. Focal mechanisms are color-coded according to the triangle diagram of Frohlich (1992), as indicated in panel (**b**). Locations of the profile A–A' to I–I' are the same as in Fig. 6. Open circles are the earthquakes located from the OBS observations. **b** Triangle diagram of Frohlich (1992) for the focal mechanisms indicated on the cross sections in panel (**c**). **c** Cross sections along the profile A–A' to I–I' on panel (**a**). Focal mechanisms and hypocenters within the dotted rectangles are indicated on each profile
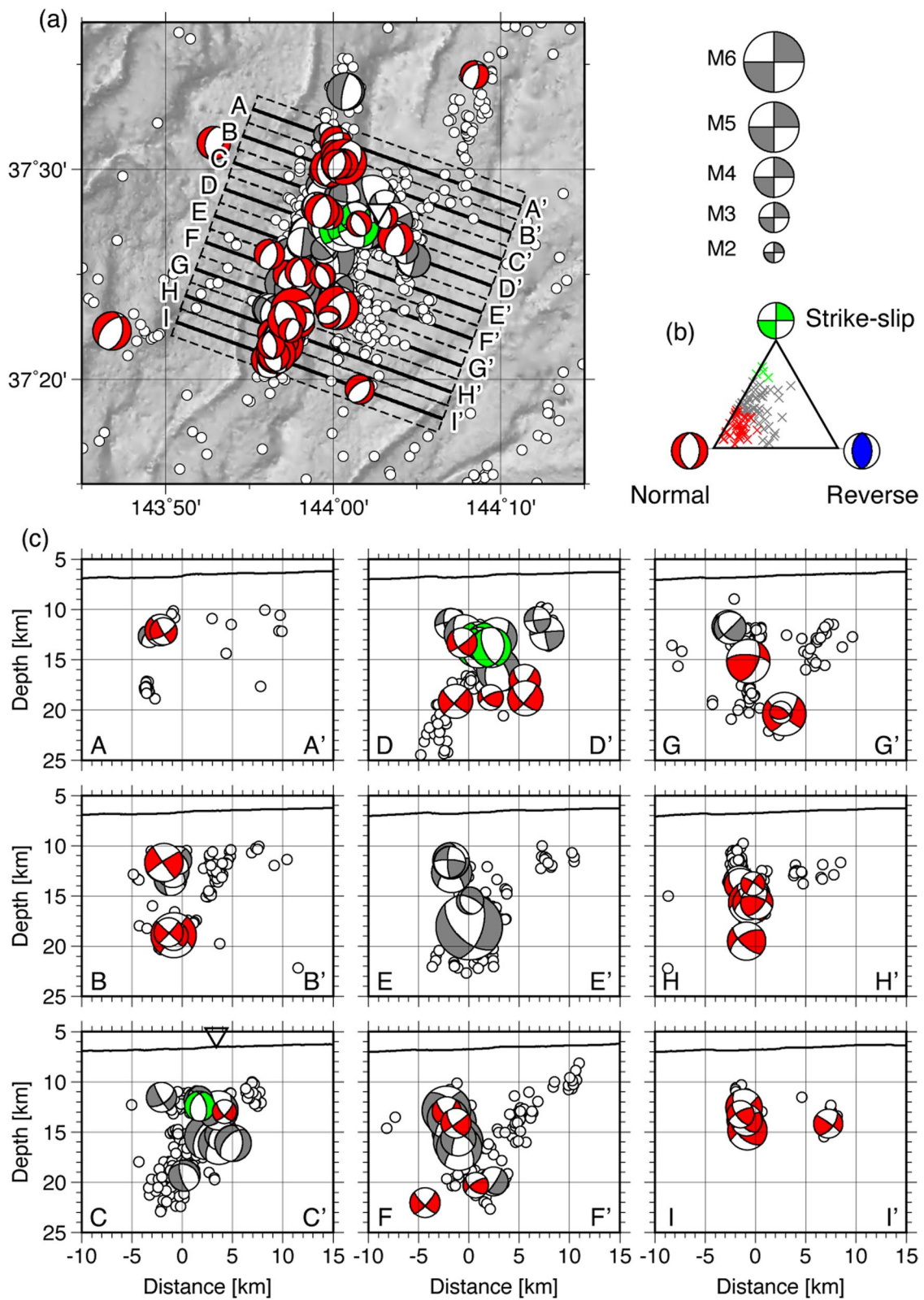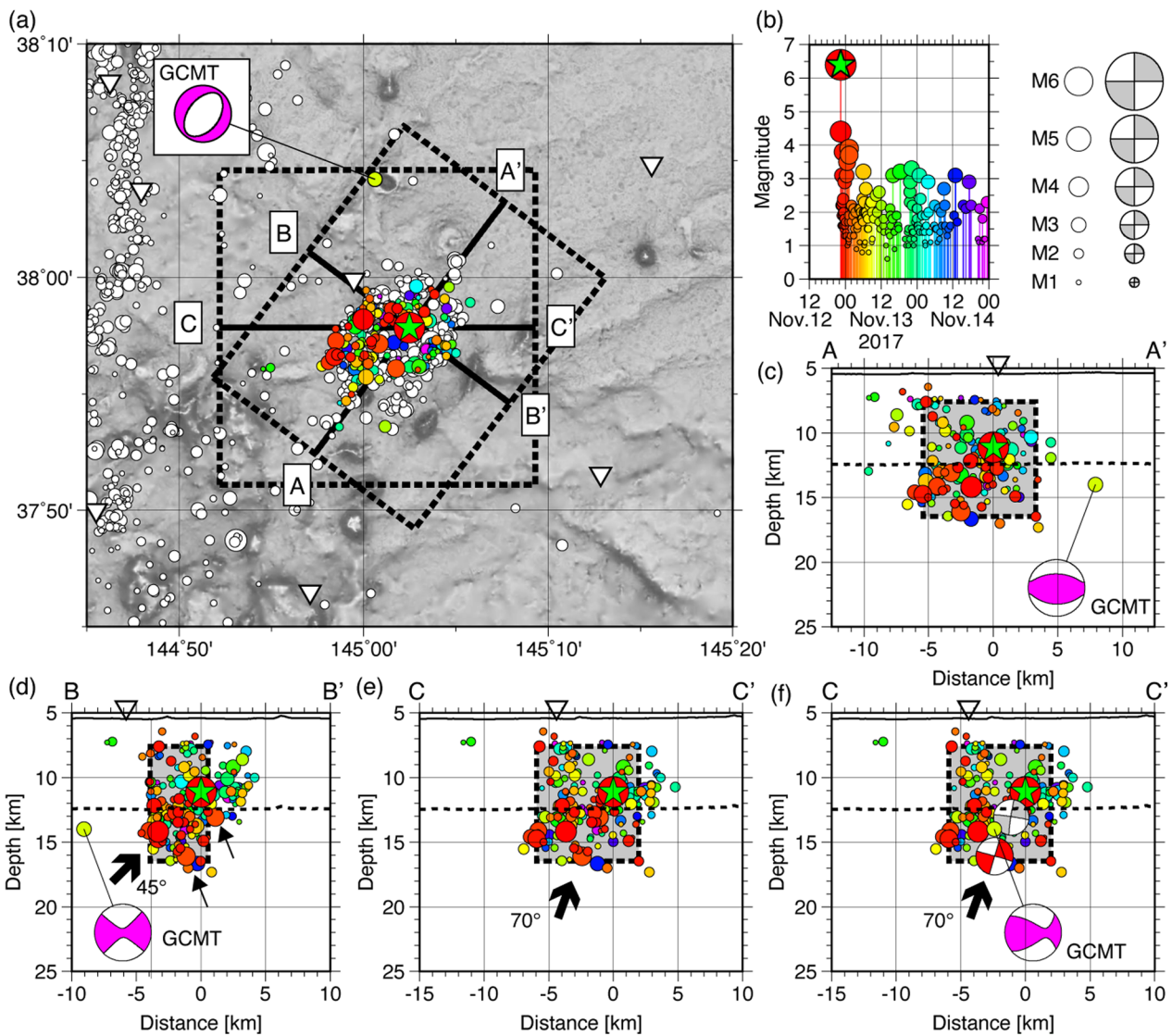
Fig. 7 (See legend on previous page.)

Fig. 8 Mainshock and aftershock activity of the November 12, 2017 earthquake. **a** Map showing the epicenter distribution of the November 12, 2017 earthquake and its aftershocks. The mainshock and its aftershocks that occurred through November 14 within the dashed rectangles are indicated by circles color-coded with time after the mainshock as indicated in panel (**b**). The mainshock is marked with a green star. The focal mechanism of the mainshock from the GCMT catalog is indicated. **b** Magnitude-time diagram of the earthquakes within the dashed rectangles on panel (**a**). **c** Cross section of the hypocenters along profile A–A' on panel (**a**). The gray rectangle indicates the area of the earthquakes that occurred within 1 h from the mainshock. **d** Cross section of the hypocenters along profile B–B' on panel (**a**). The thick arrow indicates the aftershock distribution corresponding to the northwestward-dipping plane of the GCMT solution. Thin arrows indicate the M ~4 aftershocks located below the northwestward-dipping plane. **e, f** Cross sections of the hypocenters along the profile C–C' on panel (**a**). Focal mechanisms from the OBS first-motion polarities are also indicated on panel (**f**). The focal mechanisms are color-coded by the faulting types according to the triangle diagram of Frohlich (1992), as shown in Fig. 2. Thick arrows indicate the aftershock distribution corresponding to the westward-dipping plane of the focal mechanisms from the OBS first-motion polarities

earthquakes as observed for the M6-class earthquakes in the central Japan Trench in this study. The rupture of complicated fault systems should also be considered for outer-rise earthquakes in the northern and southern sections of the Japan Trench.

5 Conclusion

Fault geometries of three M6-class outer-rise earthquakes in the Japan Trench were investigated using near-field OBS observations from September 2017 to July 2018. Off-fault aftershock activity triggered by static
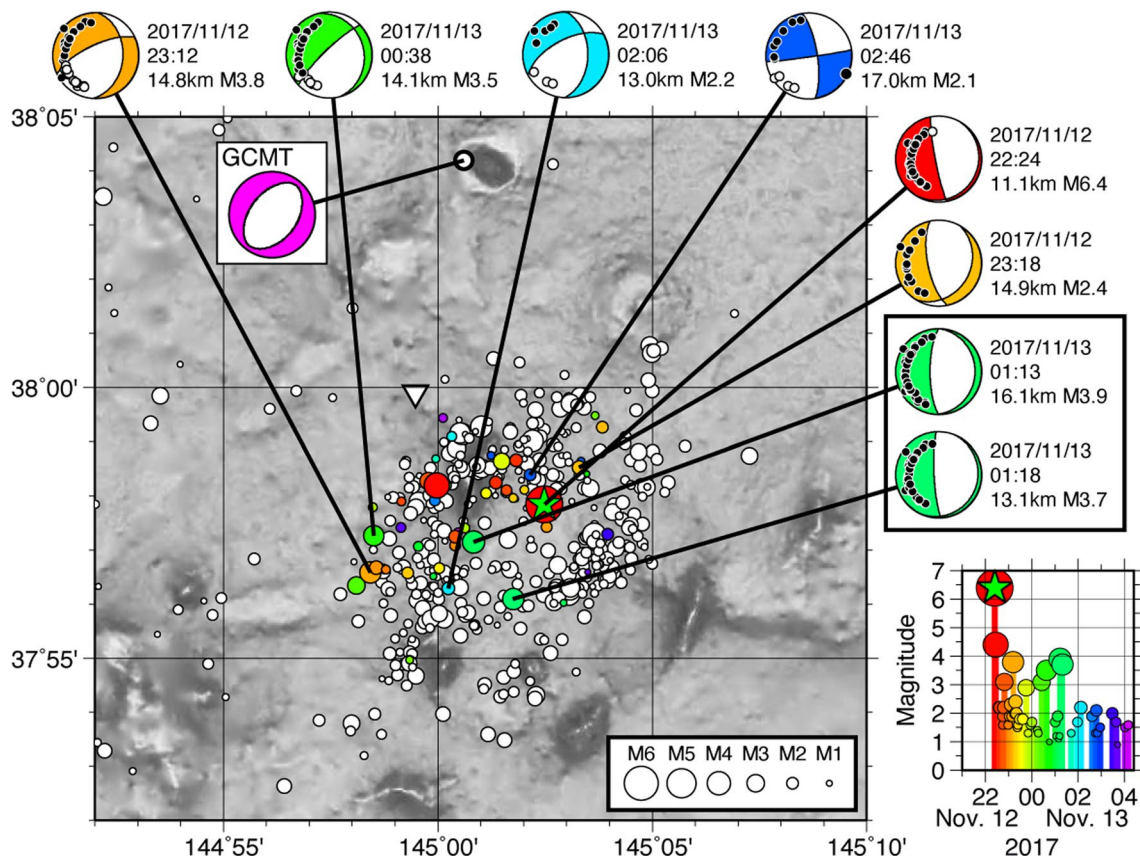
Fig. 9 Focal mechanisms and first-motion polarities of the November 12, 2017 earthquake and its aftershocks. The epicenter of the mainshock is marked with a green star. Earthquakes within 6 h from the mainshock are indicated by circles color-coded with time after the mainshock as in the magnitude-time diagram in the bottom right panel. Note that the time range differs from that in Fig. 8. Focal mechanisms are indicated with first-motion polarities. Two focal mechanisms within the solid rectangle are ranked as quality B by the HASH program (Hardebeck and Shearer 2002). The other six focal mechanisms are ranked as quality D

stress changes was observed during the September 2017 earthquake. Compound ruptures of multiple faults were proposed for the 1933 Showa-Sanriku earthquake, but this is not the case for the September 2017 earthquake, even though the overall aftershock distributions seem to be the activity of multiple faults. However, the October and November 2017 earthquake ruptures are likely related to multiple faults with complicated geometries. Early aftershocks of the October 2017 earthquake suggest that westward- and eastward-dipping faults with dip angles between 45° and 70° were associated with the mainshock rupture. In addition, the November 2017 earthquake likely relates to the abyssal hill fabrics, which were created parallel to the spreading centers, and trench-parallel normal faults formed in the outer trench slope area.

Fault geometries, such as strike orientations and dip angles, affect tsunami propagation and heights at the coast. Our near-field OBS observations show the possible complicated fault geometry of M6-class earthquakes, which ruptured a ~10-km-long fault in the central Japan Trench. Previous OBS observations in the northern and southern Japan Trench sections also showed a possible complex fault system consisting of multiple fault segments in the outer rise. In the case of large normal-faulting earthquakes, such as the 1933 Showa-Sanriku earthquake, the fault geometry could be more complex because of larger-scale rupture. In evaluating tsunamis caused by large outer-rise earthquakes, the potential of the complex geometry of the source fault consisting of multiple faults with different strikes, dip directions, and angles should be considered.
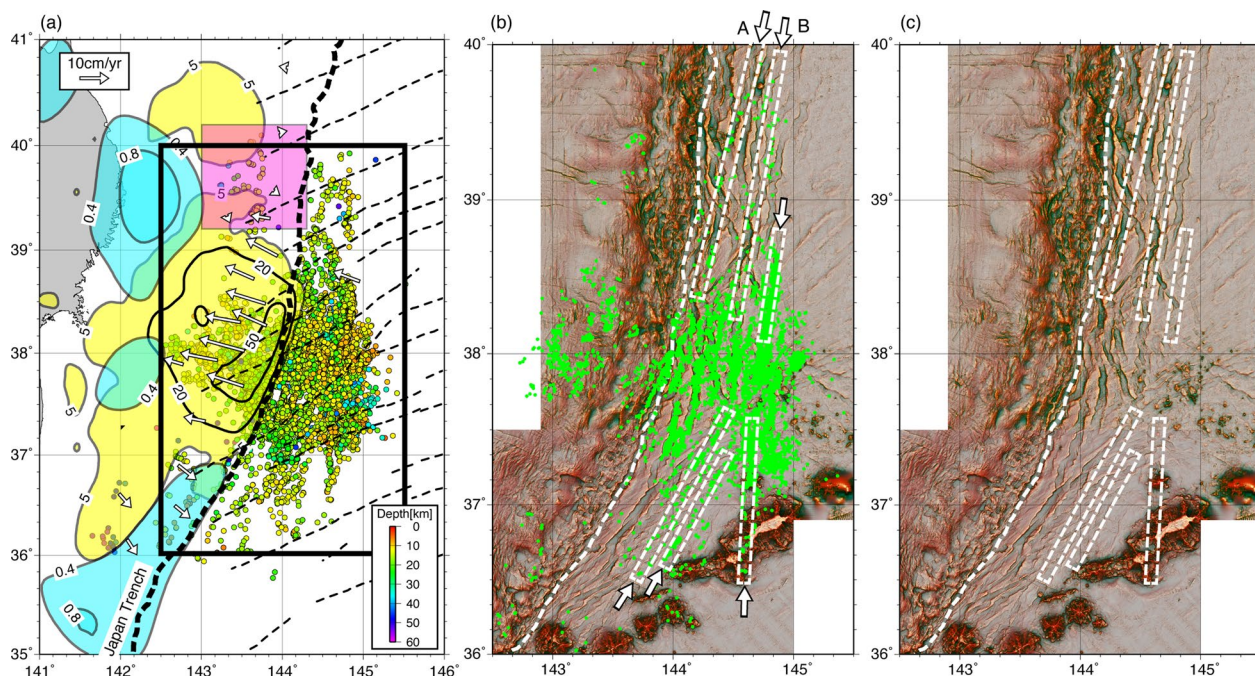
Fig. 10 Hypocenter distribution and bathymetry relief along the Japan Trench. **a** Hypocenter distribution obtained in this study and previous studies (Obana et al. 2018, 2019, 2021), represented by colored circles. The thick dashed line indicates the Japan Trench axis. Yellow and blue shaded areas indicate the coseismic (Iinuma et al. 2012) and postseismic (Iinuma et al. 2016) slip areas of the 2011 Tohoku-oki earthquake, respectively. Contours for 5-, 20-, and 50-m coseismic slip and 0.4- and 0.8-m postseismic slip are indicated. The pink rectangle and arrows indicate the slow slip event in 2015 and horizontal displacement rates relative to the North American Plate, respectively (Honsho et al. 2019). The thick solid line rectangle indicates the area shown in panels (**b**) and (**c**). **b** Red relief bathymetry map (Chiba et al. 2008) showing epicenter distribution. Green circles represent the epicenters of earthquakes shallower than 14 km obtained in this study and previous studies (Obana et al. 2018, 2019, 2021). Arrows and white dashed rectangles indicate linear earthquake trends identified in previous studies in the northern and southern sections of the Japan Trench (Obana et al. 2018, 2021). The dashed white line indicates the Japan Trench axis. **c** Red relief bathymetry map without the epicenters

Abbreviations

OBS	Ocean bottom seismograph
CMT	Centroid moment tensor
GCMT	Global centroid moment tensor
JAMSTEC	Japan Agency for Marine-Earth Science and Technology
STA/LTA	Short-term average to long-term average ratio
Vp	P-wave velocity
Vs	S-wave velocity

Supplementary Information

The online version contains supplementary material available at https://doi.org/10.1186/s40645-023-00541-7.

Additional file 1: Fig. S1. Distribution of initial hypocenters determined using 1-D velocity structure. **a** Distribution of the initial hypocenters. Colored circles are the events used for the double-difference tomographic analysis. Open and solid inverted triangles are the OBSs seaward and landward of the trench axis, respectively. **b** Cross section of the initial hypocenters along the profile X–X' shown in (**a**). **c** 1-D Vp models used for the OBSs seaward (S) and landward (L) of the trench axis. **Fig. S2.** Model configuration and initial velocity model of the tomographic analysis. **a** Map showing the initial Vp model at a depth of 15 km. Crosses indicate grid nodes of the velocity model. The red line is the survey line of Ito et al. (2005), used as a reference for the initial velocity model. Inverted triangles indicate the OBS locations. Bathymetric contours in meters. **b** Cross section of the initial Vp model along axis X. Dashed black lines indicate the top of the oceanic crust (Ito et al. 2005) and the approximate depth of

the Moho, which is 7 km below the seafloor seaward of the trench and 6 km below the top of the oceanic crust landward of the trench. Inverted triangles indicate the projected locations of OBSs. White contours are iso-velocity contours of Vp. **Fig. S3.** Results of the tomographic analysis and checkerboard resolution test. **a** Map showing the obtained Vp model at a depth of 15 km. Symbols are the same as in Fig. S2. **b, c** Cross sections of Vp (**b**) and Vs (**c**) model along the profile X–X' on panel (**a**). **d** Map showing the results of the checkerboard resolution test for Vp at a depth of 15 km. **e, f** Cross sections of the results for Vp (**e**) and Vs (**f**) along the profile X–X' on panel (**d**). **Fig. S4.** Location errors of the hypocenters estimated from 100 bootstrap samples. **a** Map showing error ellipsoids of hypocenter locations. Error ellipsoids are color-coded by location errors. Open stars are the epicenter of three M6-class earthquakes. **b** Cross section of hypocenter errors projected along the profile indicated by a thick solid line on panel (**a**). **Fig. S5.** Temporal evolution of aftershock activity for the first 24 h of the September 20, 2017 earthquake. **a**–**f** Maps and cross sections showing aftershock hypocenters for each time range, represented with circles. The origin time of the mainshock is 16:37. Aftershocks within the first hour of the mainshock are indicated in panel (**a**). Green stars indicate the hypocenter location of the mainshock. The time ranges displayed on each panel vary from 1 to 8 h. Cross sections indicate hypocenters projected along the thick solid line on the map, which represents profile A–A' in Fig. 3. Inverted triangles indicate the OBS locations. The seafloor and the approximate depth of the Moho, 7 km below the seafloor, are indicated on the cross sections with solid and dashed lines, respectively. **Fig. S6.** Coulomb stress changes at aftershock hypocenters for the September 20, 2017 earthquake. **a** Map and cross section indicating the definition of the west, mainshock, and east areas used in panel (**b**). Green stars are

Obana *et al. Progress in Earth and Planetary Science*   (2023) 10:11

Page 18 of 19

the hypocenter of the mainshock. The green rectangle on the map view and thick green line on the cross section are the assumed faults of the mainshock for case 1, in which the rupture extends both in the oceanic crust and uppermost oceanic mantle. Inverted triangles indicate the OBS locations. Open circles are the aftershocks that occurred until September 22, 2017, which are the same as the colored events in Fig. 3. **b** Frequency distribution of Coulomb stress changes (dCFF) at aftershock hypocenters. The stress changes on both westward and eastward-dipping normal faults with a 70° dipping angle were calculated for the aftershocks that occurred within the map area in panel (**a**) until September 22, 2017.

Additional file 2: Table S1. Coulomb stress changes (dCFF) for the aftershocks of the September 20, 2017 earthquake. The stress changes for the aftershocks occurred within the map area in Additional file 1: Fig. S6a until September 22, 2017 have been examined.

Availability of data and materials
The OBS data underlying this article are available in the JAMSTEC Seismic Survey Database, at https://doi.org/10.17596/0002069. The global CMT catalog (Dziewonski et al. 1981; Ekström et al. 2012) is available at https://www.globalcmt.org. All other data are available from the corresponding author upon request.

Declarations

Competing interests
The authors declare that they have no competing interests.

References
Abe K (1978) A dislocation model of the 1933 Sanriku earthquake consistent with the tsunami waves. J Phys Earth 26(4):381–396. https://doi.org/10.4294/jpe1952.26.381

Álvarez-Gómez JA, Gutiérrez Gutiérrez OQ, Aniel-Quiroga Í, González M (2012) Tsunamigenic potential of outer-rise normal faults at the Middle America trench in Central America. Tectonophysics 574–575:133–143. https://doi.org/10.1016/j.tecto.2012.08.014

Asano Y, Saito T, Ito Y, Shiomi K, Hirose H, Matsumoto T, Aoi S, Hori S, Sekiguchi S (2011) Spatial distribution and focal mechanisms of aftershocks of the 2011 off the Pacific coast of Tohoku Earthquake. Earth Planets Space 63(7):669–673. https://doi.org/10.5047/eps.2011.06.016

Baba T, Chikasada N, Nakamura Y, Fujie G, Obana K, Miura S, Kodaira S (2020) Deep investigations of outer-rise tsunami characteristics using

well-mapped normal faults along the Japan Trench. J Geophys Res Solid Earth 125(10):e2020JB020060. https://doi.org/10.1029/2020jb020060

Chiba T, Kaneta S, Suzuki Y (2008) Red relief image map: new visualization method for three dimensional data. Int Arch Photogramm Remote Sens Spat Inf Sci 37(B2):1071–1076

Das S, Henry C (2003) Spatial relation between main earthquake slip and its aftershock distributions. Rev Geophys 41(3):1013. https://doi.org/10.1029/2002RG000119

Dziewonski AM, Chou T-A, Woodhouse JH (1981) Determination of earthquake source parameters from waveform data for studies of global and regional seismicity. J Geophys Res 86(B4):2825–2852. https://doi.org/10.1029/JB086iB04p02825

Ekström G, Nettles M, Dziewoński A (2012) The global CMT project 2004–2010: centroid-moment tensors for 13,017 earthquakes. Phys Earth Planet Inter 200–201:1–9. https://doi.org/10.1016/j.pepi.2012.04.002

Frohlich C (1992) Triangle diagrams: ternary graphs to display similarity and diversity of earthquake focal mechanisms. Phys Earth Planet Inter 75(1–3):193–198

Hardebeck JL, Shearer PM (2002) A new method for determining first-motion focal mechanisms. Bull Seismol Soc Am 92:2264–2276. https://doi.org/10.1785/0120010200

Harris RA (1998) Introduction to special section: Stress triggers, stress shadows, and implications for seismic hazard. J Geophys Res Solid Earth 103(B10):24347–24358. https://doi.org/10.1029/98JB01576

Headquarters for Earthquake Research Promotion (2009) Seismic activity in Japan—regional perspectives on the characteristics of destructive earthquakes, 2nd edn. Association for the Development of Earthquake Prediction. (**in Japanese**)

Hino R, Azuma R, Ito Y, Yamamoto Y, Suzuki K, Tsushima H, Suzuki S, Miyashita M, Tomori T, Arizono M, Tange G (2009) Insight into complex rupturing of the immature bending normal fault in the outer slope of the Japan Trench from aftershocks of the 2005 Sanriku earthquake (Mw = 7.0) located by ocean bottom seismometry. Geochem Geophys Geosyst 10(7):Q07O18. https://doi.org/10.1029/2009GC002415

Hirata N, Matsu'ura M (1987) Maximum-likelihood estimation of hypocenter with origin time eliminated using nonlinear inversion technique. Phys Earth Planet Inter 47:50–61

Hjörleifsdóttir V, Ekström G (2010) Effects of three-dimensional earth structure on CMT earthquake parameters. Phys Earth Planet Inter 179(3):178–190. https://doi.org/10.1016/j.pepi.2009.11.003

Honsho C, Kido M, Tomita F, Uchida N (2019) Offshore postseismic deformation of the 2011 Tohoku earthquake revisited: application of an improved GPS-acoustic positioning method considering horizontal gradient of sound speed structure. J Geophys Res Solid Earth 124(6):5990–6009. https://doi.org/10.1029/2018jb017135

Iinuma T, Hino R, Kido M, Inazu D, Osada Y, Ito Y, Ohzono M, Tsushima H, Suzuki S, Fujimoto H, Miura S (2012) Coseismic slip distribution of the 2011 off the Pacific Coast of Tohoku Earthquake (M9.0) refined by means of seafloor geodetic datas. J Geophys Res 117(B7):B07409. https://doi.org/10.1029/2012JB009186

Iinuma T, Hino R, Uchida N, Nakamura W, Kido M, Osada Y, Miura S (2016) Seafloor observations indicate spatial separation of coseismic and postseismic slips in the 2011 Tohoku earthquake. Nat Commun 7(1):13506. https://doi.org/10.1038/ncomms13506

Ito A, Fujie G, Miura S, Kodaira S, Kaneda Y, Hino R (2005) Bending of the subducting oceanic plate and its implication for rupture propagation of large interplate earthquakes off Miyagi, Japan, in the Japan Trench subduction zone. Geophys Res Lett 32:L05310. https://doi.org/10.1029/2004GL022307

JHOD, JAMSTEC (2011) Bathymetry data off Tohoku, Japan. Seismol Soc Jpn News Lett 23(2):35–36 (**in Japanese**)

Kanamori H (1971) Seismological evidence for a lithospheric normal faulting: the Sanriku earthquake of 1933. Phys Earth Planet Inter 4:289–300

Kido Y, Fujiwara T, Sasaki T, Kinoshita M, Kodaira S, Sano M, Ichiyama Y, Hanafusa Y, Tsuboi S (2011) Bathymetric feature around Japan Trench obtained by JAMSTEC multi narrow beam survey. JpGU meeting 2011 Abstract MIS036-P58 presented at Japan Geoscience Union Meeting 2011, Chiba, Japan, 20–25 May 2011

Kubota T, Hino R, Inazu D, Ito Y, Iinuma T (2015) Complicated rupture process of the Mw 7.0 intraslab strike-slip earthquake in the Tohoku region on

10 (2011) revealed by near-field pressure records. Geophys Res Lett 42(22):9733–9739. https://doi.org/10.1002/2015GL066101

Lay T, Ammon C, Kanamori H, Kim M, Xue L (2011) Outer trench-slope faulting and the 2011 Mw 9.0 off the Pacific coast of Tohoku Earthquake. Earth Planets Space 63(7):713–718. https://doi.org/10.5047/eps.2011.05.006

Lay T, Ye L, Wu Z, Kanamori H (2020) Macrofracturing of oceanic lithosphere in complex large earthquake sequences. J Geophys Res Solid Earth 125(10):e2020JB020137. https://doi.org/10.1029/2020JB020137

Nakamura W, Uchida N, Matsuzawa T (2016) Spatial distribution of the faulting types of small earthquakes around the 2011 Tohoku-oki earthquake: a comprehensive search using template events. J Geophys Res 121(4):2591–2607. https://doi.org/10.1002/2015JB012584

Nakanishi M (2011) Bending-related topographic structures of the subducting plate in the northwestern Pacific Ocean. In: Ogawa Y, Anma R, Dilek Y (eds) Accretionary prisms and convergent margin tectonics in the Northwest Pacific Basins. Modern approaches in solid earth sciences, vol 8. Springer, Dordrecht, pp 1–38. https://doi.org/10.1007/978-90-481-8885-7_1

Obana K, Fujie G, Takahashi T, Yamamoto Y, Nakamura Y, Kodaira S, Takahashi N, Kaneda Y, Shinohara M (2012) Normal-faulting earthquakes beneath the outer slope of the Japan Trench after the 2011 Tohoku earthquake: implications for the stress regime in the incoming Pacific plate. Geophys Res Lett 39:L00G24. https://doi.org/10.1029/2011GL050399

Obana K, Kodaira S, Shinohara M, Hino R, Uehira K, Shiobara H, Nakahigashi K, Yamada T, Sugioka H, Ito A, Nakamura Y, Miura S, No T, Takahashi N (2013) Aftershocks near the updip end of the 2011 Tohoku-Oki earthquake. Earth Planet Sci Lett 382:111–116. https://doi.org/10.1016/j.epsl.2013.09.007

Obana K, Takahashi T, No T, Kaiho Y, Kodaira S, Yamashita M, Sato T, Nakamura T (2014) Distribution and migration of aftershocks of the 2010 Mw 7.4 Ogasawara Islands intraplate normal-faulting earthquake related to a fracture zone in the Pacific plates. Geochem Geophys Geosyst 15(4):1363–1373. https://doi.org/10.1002/2014GC005246

Obana K, Nakamura Y, Fujie G, Kodaira S, Kaiho Y, Yamamoto Y, Miura S (2018) Seismicity in the source areas of the 1896 and 1933 Sanriku earthquakes and implications for large near-trench earthquake faults. Geophys J Int 212(3):2061–2072. https://doi.org/10.1093/gji/ggx532

Obana K, Fujie G, Takahashi T, Yamamoto Y, Tonegawa T, Miura S, Kodaira S (2019) Seismic velocity structure and its implications for oceanic mantle hydration in the trench-outer rise of the Japan Trench. Geophys J Int 217(3):1629–1642. https://doi.org/10.1093/gji/ggz099

Obana K, Fujie G, Yamamoto Y, Kaiho Y, Nakamura Y, Miura S, Kodaira S (2021) Seismicity around the trench axis and outer-rise region of the southern Japan Trench, south of the main rupture area of the 2011 Tohoku-oki earthquake. Geophys J Int 226(1):131–145. https://doi.org/10.1093/gji/ggab093

Okada Y (1992) Internal deformation due to shear and tensile faults in a half-space. Bull Seismol Soc Am 82(2):1018–1040. https://doi.org/10.1785/BSSA0820021018

Olson CJ, Becker JJ, Sandwell DT (2016) SRTM15_PLUS: data fusion of Shuttle Radar Topography Mission (SRTM) land topography with measured and estimated seafloor topography (NCEI Accession 0150537). NOAA National Centers for Environmental Information. https://www.ncei.noaa.gov/archive/accession/0150537. Accessed 9 Feb 2021

Park J-O, Takahata N, Jamali Hondori E, Yamaguchi A, Kagoshima T, Tsuru T, Fujie G, Sun Y, Ashi J, Yamano M, Sano Y (2021) Mantle-derived helium released through the Japan trench bend-faults. Sci Rep 11(1):12026. https://doi.org/10.1038/s41598-021-91523-6

Sladen A, Trevisan J (2018) Shallow megathrust earthquake ruptures betrayed by their outer-trench aftershocks signature. Earth Planet Sci Lett 483:105–113. https://doi.org/10.1016/j.epsl.2017.12.006

Sun T, Wang K, Fujiwara T, Kodaira S, He J (2017) Large fault slip peaking at trench in the 2011 Tohoku-oki earthquake. Nat Commun 8:14044. https://doi.org/10.1038/ncomms14044

Tanioka Y, Satake K (1996) Fault parameters of the 1896 Sanriku tsunami earthquake estimated from tsunami numerical modeling. Geophys Res Lett 23(13):1549–1552

Toda S, Lin J, Stein R (2011) Using the 2011 Mw 9.0 off the Pacific coast of Tohoku Earthquake to test the Coulomb stress triggering hypothesis and to calculate faults brought closer to failures. Earth Planets Space 63(7):725–730. https://doi.org/10.5047/eps.2011.05.010

Uchida N, Kirby SH, Umino N, Hino R, Kazakami T (2016) The great 1933 Sanriku-oki earthquake: reappraisal of the main shock and its aftershocks and implications for its tsunami using regional tsunami and seismic datas. Geophys J Int 206(3):1619–1633. https://doi.org/10.1093/gji/ggw234

Urabe T, Tsukada S (1992) Win: a workstation program for processing waveform data from microearthquake networks. Programme and Abstracts, The seismological society of Japan No. 2:P–41. (**in Japanese**)

Wang K, Sun T, Brown L, Tomita F, Hino R, Kido M, Kodaira S, Iinuma T, Fujiwara T (2018) Learning from crustal deformation associated with the M9 2011 Tohoku-oki earthquake. Geosphere 14(2):552–571. https://doi.org/10.1130/GES01531.1

Watanabe H (1971) Determination of earthquake magnitude at regional distance in and near Japan. Zisin (J Seismol Soc Jpn) 24:189–200 (**in Japanese with English abstract**)

Wells DL, Coppersmith KJ (1994) New empirical relationships among magnitude, rupture length, rupture width, rupture area, and surface displacement. Bull Seismol Soc Am 84(4):974–1002. https://doi.org/10.1785/BSSA0840040974

Zhang H, Thurber CH (2003) Double-difference tomography: the method and its application to the Hayward Fault, California. Bull Seismol Soc Am 93(5):1875–1889

Publisher's Note